

1 Spatiotemporal scales of mode water transformation in the Sea of

2 Oman

3 Estel Font¹, Esther Portela², Sebastiaan Swart^{1,3}, Mauro Pinto-Juica¹, Bastien Y. Queste¹

4 ¹Department of Marine Sciences, University of Gothenburg, Gothenburg, Sweden

5 ²Laboratoire d'Océanographie Physique et Spatiale, University of Brest, CNRS, IRD, Ifremer, Plouzané, France

6 ³Department of Oceanography, University of Cape Town, Rondebosch, South Africa

8 *Correspondence to:* Estel Font (estel.font.felez@gu.se)

9 **Abstract.** In the Sea of Oman, mode water forms at the surface and is trapped under a warm stratified layer in summer. This
10 capped and well-mixed oxygenated layer decouples the oxygen minimum zone from ocean surface processes. It also provides
11 a space for remineralisation, reducing oxygen demand in the oxygen minimum zone. Several physical processes, from
12 isopycnal and diapycnal mixing to advection, transform mode water and change its properties. We perform a volume budget
13 analysis to investigate the mechanisms driving mode water volume change in the Sea of Oman from monthly to 3-day temporal
14 scales using monthly climatologies derived from profiling floats and high-resolution underwater glider observations. Isopycnal
15 and diapycnal water-mass transformations are estimated in a density-spice framework. Our study shows that mode water
16 predominantly transforms along isopycnals, yet strong but transient diapycnal transformation occurs at shorter timescales.
17 Moreover, fluxes between the mode water layer and its surroundings are highly sensitive to the presence of mesoscale eddies.
18 Across eddies, diapycnal and isopycnal transformations intensify by 61% and 45% respectively, compared to non-eddy
19 conditions, indicating that eddies are drivers of both lateral and vertical water mass exchanges. This study provides a novel
20 application of the water mass transformation framework to high-resolution underwater gliders, and shows that this
21 methodology can be used at higher resolution than traditional climatological products or models. By comparing monthly
22 climatological products to the high-resolution glider data, we suggest that the climatological estimates are outside of the high-
23 resolution glider mean \pm standard error 40% of the time for diapycnal and 60% of the time for isopycnal transformation. These
24 results highlight the intense variability occurring at small scales and can serve to inform future estimates of water mass
25 transformation uncertainty from coarser products.

26 1 Introduction

27 Mode waters are vertically homogeneous waters formed in the surface mixed layer and then subducted into the ocean interior
28 (Hanawa and Talley, 2001). Surface water properties and tracers (e.g, heat, oxygen, organic matter) are trapped below the

29 mixed layer during mode water formation. The seasonal variations of the mixed layer result in alternating mixing and
30 stratification periods, trapping mode waters in the ocean subsurface, and favoring heat uptake, carbon sequestration, and
31 oxygen ventilation (Lacour et al., 2023; Li et al., 2023; Portela et al., 2020a). Thus, mode water plays a crucial role as a
32 pathway connecting the surface and subsurface ocean, influencing the distribution and transport of oxygen, heat, and
33 remineralized organic matter.

34

35 In the Sea of Oman, mode water forms when springtime warming and weak turbulent fluxes stratify the surface layer and cap
36 the deep surface mixed layer formed during the winter monsoon (Font et al., 2022, 2025; Senafi et al., 2019). The fate of mode
37 water determines whether subducted surface properties are retained and transported into the ocean interior or mixed back into
38 the surface mixed layer. This fate is governed by a variety of complex physical processes and instabilities that act at different
39 spatial and temporal scales, resulting in diapycnal and isopycnal mixing and advection of mode water properties. Thus, these
40 processes collectively regulate the transformation, ventilation, and residence time of mode water, thereby controlling its
41 capacity to act as an oxygen reservoir (Kalvelage et al., 2015), or as a remineralization buffer layer (Weber and Bianchi, 2020).

42

43 In the Sea of Oman, mode water volume and residence time are among the largest within the Arabian Sea (thickness > 50 m
44 and residence time > 4 months; Font et al., 2025), making it a key reservoir of oxygen. Mode water provides significant
45 opportunities for the remineralization of labile sinking organic matter within this layer, reducing biological oxygen demand in
46 the core of the oxygen minimum zone (Weber and Bianchi, 2020). Moreover, these are oxygen-rich waters, which can sustain
47 the oxygen supplied to the upper oxygen minimum zone across the oxycline. It has been shown that, for instance, 50% of the
48 oxygen changes along mode water ventilation pathways are due to net community respiration within the water mass, the rest
49 being due to mixing with surrounding oxygen-poorer waters (Jutras et al., 2025). Given their role in ocean heat uptake,
50 biogeochemical cycling, and carbon sequestration, the life cycle of mode water and its changes have significant implications
51 for both regional and global ocean-climate dynamics. Understanding the physical processes that mix and stratify mode water
52 across scales, and how these processes interact with biogeochemical dynamics, is critical. While Font et al. (2025) provide
53 valuable estimates of mode-water volume and residence time, the subseasonal and small-scale variability that governs changes
54 in its properties remains poorly constrained, largely because observations at the necessary spatiotemporal resolution are still
55 scarce.

56

57 Based on the method first introduced by Walin (1982) to compute water-mass transformation in thermohaline coordinates, we
58 use a density-spice (σ - τ) framework (Portela et al., 2020b) to investigate volume changes at timescales, from daily to monthly,
59 of mode water in the Sea of Oman leveraging high spatio-temporal resolution from underwater glider observations and Argo
60 monthly climatologies. Potential density is used because it is materially conserved under adiabatic and isohaline motions and
61 therefore provides a practical approximation to separate isopycnal and diapycnal fluxes, while spice is added as a second
62 dimension in the volume budget to identify different water masses spreading along isopycnals (Jackett and McDougall, 1985;

63 McDougall and Krzysik, 2015). Spice acts as a tracer of thermohaline changes along isopycnals, enabling the identification of
64 water masses that are indistinguishable in density but differ in origin or transformation history. The water mass transformation
65 framework has been widely employed to quantify how water masses change properties over seasonal to interannual timescales,
66 often using Argo float data or numerical models (Badin et al., 2013; Evans et al., 2014; Nurser et al., 1999; Portela et al.,
67 2020b). These studies reveal gradual seasonal transformation driven by surface fluxes and large-scale circulation. However,
68 evidence highlights the significant contribution of mesoscale eddies and other transient processes to shorter-term variability
69 and transformation events (e.g., Liu et al., 2013; Shi et al., 2018; Trott et al., 2019; Thoppil, 2024; Xu et al., 2016). Our
70 approach and a high-resolution dataset allow us to capture the episodic and localized transformations often missed by coarser-
71 resolution climatologies and models, to resolve short-term drivers of isopycnal and diapycnal change.

72

73 Specifically, this study addresses the following key questions: (1) How does mode water change across different timescales,
74 from days to seasons? (2) Which physical mechanisms predominantly drive mode water transformations in the Sea of Oman?
75 By combining glider data with climatological products, we provide a quantitative assessment of water mass transformation
76 dynamics of this layer with important biogeochemical regional implications.

77 **2. Data and methods**

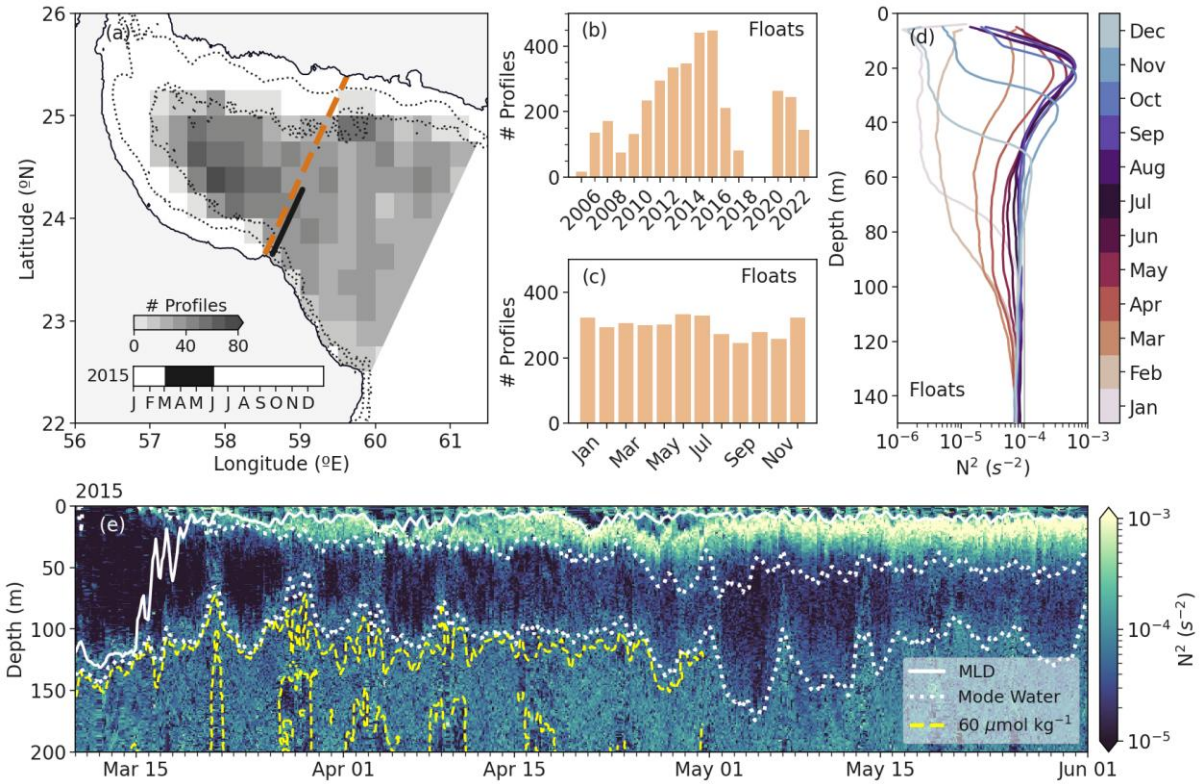
78 **2.1 Ocean glider observations and Argo climatology**

79 We utilized four months of glider observations sampling across the continental shelf in the southern Sea of Oman. The
80 Seaglider carried out repeated sampling along an 80-km transect between 23.65°N, 58.65°E and 24.25°N, 59°E in 2015 (Figure
81 1a). Observations were projected onto a straight across-shelf transect (Figure 1a, black line) and median-binned onto a 0.5 m
82 (vertical) and 2 km (horizontal) grid. The origin of coordinates was taken at the 300 m isobath. Binned sections were
83 interpolated vertically (1 m), then horizontally (4 km) to fill minor gaps, and smoothed horizontally with a 6 km running mean.
84 The 6 km running mean is selected as a compromise between filtering out submesoscale variability ($\lesssim O(10)$ km) and
85 preserving mesoscale structures ($\gtrsim O(20)$ km), comparable to the local Rossby radius. Mixed layer depth was defined using a
86 potential density threshold of 0.125 kg m^{-3} relative to the surface (Font et al., 2022). Spice (τ ; kg m^{-3}) was computed from
87 Conservative Temperature (Graham and McDougall, 2013; McDougall, 2003) and Absolute Salinity (McDougall et al., 2012)
88 following the TEOS-10 routines (gsw_spiciness0; McDougall and Barker, 2011). Potential density and spice are referenced at
89 0 dbar. Eddy kinetic energy (EKE) was estimated from two independent sources: (1) the depth-averaged currents (DAC)
90 derived from the glider flight model as $EKE = (DAC - \overline{DAC})^2$, where \overline{DAC} is the mean DAC during the glider campaign
91 (Frajka-Williams et al., 2011); and (2) from sea surface height-derived surface geostrophic velocities from satellite (CMEMS,
92 2025). EKE is defined as $u'^2 + v'^2$; where $u' = u - \bar{u}$ and $v' = v - \bar{v}$ are respectively the zonal and meridional velocity time
93 anomalies, where u and v are the surface geostrophic velocities at the glider transect location and \bar{u} and \bar{v} are the mean surface
94 geostrophic velocities during the glider-sampling period. Mesoscale eddies in the region were identified using the ToEddies

95 dataset, which applies an eddy detection algorithm to satellite-derived Absolute Dynamic Topography (ADT) fields (Laxenaire
96 et al., 2024). The dataset provides daily information on eddy properties, including polarity, center location, and spatial extent
97 (Laxenaire et al., 2024; Ioannou et al., 2024).

98
99 In addition, we used a total of 3565 Argo profiles of temperature, salinity, and pressure between 2000 and 2023 in the Sea of
100 Oman (22.5-26 °N, 56-61°E, Figure 1a). Only profiles flagged as “good” by the CORIOLIS Data Centre were used (Gaillard
101 et al., 2009). Argo float coverage spans the entire domain, with an average density of 28 profiles per $0.25^\circ \times 0.25^\circ$ grid cell
102 (Figure 1a) and a relatively uniform monthly distribution (Figure 1c). Argo profiles within a 200 km distance from the across-
103 Sea of Oman transect (Figure 1a, orange dashed line) were selected. This strategy ensures sufficient monthly sampling
104 coverage in this sparsely observed region to construct an across-gulf monthly climatology. Moreover, to avoid the influence
105 of shallow profiles on the continental shelf, profiles shallower than 1000 m were excluded, so the transect remains
106 representative of the environment where mode water forms and persists. Each profile was then orthogonally projected onto the
107 nearest point along the transect (the orange dashed line in Figure 1a), which provides its along-transect coordinate. Profiles
108 were vertically interpolated onto a uniform 2-m pressure grid, and all projected profiles were median-binned into 3-km
109 horizontal bins along the transect. Averaging was performed on pressure levels. Monthly climatologies were produced by
110 taking the median across all profiles within each (depth, distance) bin for each month between 2000 and 2023. This gridded
111 product is then used as input for the σ - τ water-mass transformation calculations.
112

113 We defined the mode water core as the layer bounded by the 25 and 25.25 kg m^{-3} isopycnals, which effectively capture the
114 low-stratification and low-potential vorticity typical of mode water. This density-based definition closely aligns with a more
115 traditional identification based on potential vorticity (Feucher et al., 2022; Herraiz-Borreguero and Rintoul, 2011; McCartney,
116 1982), as demonstrated by a strong correlation between potential vorticity and the potential density threshold method (see
117 Figure S1; mode water thickness correlation between methods is $r^2 = 0.96$). Using a fixed isopycnal threshold simplifies the
118 interpretation of water mass transformation processes within the σ - τ framework (see Section 2.2), while remaining consistent
119 with dynamically meaningful definitions of mode water.
120



121

122
123
124
125
126
127
128
129

Figure 1: Data distribution. (a) Sea of Oman colored by the number of Argo profiles per $0.25^\circ \times 0.25^\circ$ geographical grid. Land is shaded gray, the coastline is marked as a solid line, and the contours of the 100 m and 1000 m isobaths are dotted. The dashed orange line is the transect across the Sea of Oman where Argo profiles are projected to. The glider transect is marked with the black line, and its duration is colored in black in the time bar. (b) Yearly and (c) monthly distribution of the number of Argo profiles in the Sea of Oman. (d) Monthly climatological stratification (Brunt-Vaisala frequency squared, N^2) profiles from Argo data. (e) Stratification time series of the upper 200 m from the glider data. The white solid line is the mixed layer depth, the upper and lower boundaries of the mode water layer (25 and 25.25 kg m^{-3} isopycnals, respectively) are marked with white dotted contours, and the yellow dashed line is the $60 \mu\text{mol kg}^{-1}$ oxygen contour. Note that after May, no more oxygen data are available due to sensor failure.

130

2.2 Water mass transformation framework

131
132
133
134
135

The analyses are performed in σ - τ coordinates since: (1) potential density is the natural coordinate to study ocean dynamics and provides information about the diapycnal nature of the mechanisms driving the volume change; and (2) spice is interpreted as a measure of thermohaline variability along isopycnals, reflecting isopycnally-compensated temperature and salinity changes associated with the spreading of distinct water masses (Jackett and McDougall, 1985; McDougall and Krzysik, 2015).

136
137
138
139

Based on the constructed Argo monthly climatology and the ocean glider dataset, we performed a volume budget in σ - τ coordinates for the interior ocean (i.e., below the mixed layer). The water-mass volume change dV/dt results from the sum of water-mass transformation, $\sum U(\sigma, \tau)$, and the exchange flux across the domain's geographical limits Ψ (Figure 2a and Equation 1; Evans et al., 2014; Portela et al., 2020b). U is the water-mass transformation due to isopycnal and diapycnal mixing fluxes,

140 whereas its convergence or divergence is represented by the sum (\sum) of the interior fluxes across the geographical limits of a
 141 given a σ - τ class (Donners et al. 2005; Walin 1982). The isopycnal and diapycnal transformation rates represent the net mixing
 142 of water masses along and across density surfaces, respectively, resulting in an irreversible property change. Ψ represents the
 143 net exchange across the northern boundary of the domain, defined as the northernmost bin of the glider and climatology
 144 transect. Since the southern end is shelf-constrained, cross-section exchange there is assumed to be negligible. Note that an
 145 underestimation of the exchange flux Ψ could result in an apparent overestimation of the local transformation rate U . However,
 146 since both diapycnal and isopycnal transformations are estimated using the same underlying framework, there is no reason to
 147 expect a preferential bias toward either component. A diagram illustrating how changes in water characteristics are represented
 148 in σ - τ space is shown in Figure 2a. The processes that modify the volume of a σ - τ class are depicted in geographical coordinates
 149 in Figures 2b-c. The σ - τ class highlighted with a square in Figure 2a is marked with dots in Figures 2b-c. In summary, changes
 150 in volume within a given σ - τ class can be attributed to the convergence or divergence of interior fluxes across σ or τ boundaries,
 151 or via exchange fluxes across the domain boundaries within the same σ - τ class. Unlike interior mixing, exchange fluxes do not
 152 imply a transformation of water mass properties.

153
 154 The method used here to compute water-mass transformation in the σ - τ coordinates is based on Portela et al. (2020b) and Evans
 155 et al. (2014). The volume change within a given σ - τ class can be expressed as:

156
$$\frac{dV}{dt}(\sigma', \tau') = U_\sigma(\sigma', \tau') + U_\tau(\sigma', \tau') + \Psi(\sigma', \tau') \quad [1]$$

157 where

158
$$U_\sigma(\sigma, \tau) = \int_{\sigma'=\sigma} \Pi(\tau, \tau') \cdot u_\sigma \cdot dA \quad \text{and} \quad U_\tau(\sigma, \tau) = \int_{\tau'=\tau} \Pi(\sigma, \sigma') \cdot u_\tau \cdot dA ; \quad [2.1, 2.2]$$

159 Where u_σ and u_τ are the diapycnal and isopycnal (diaspice) velocity components, respectively, and dA is the cross-sectional
 160 area of the transect occupied by water within the specified σ - τ class. Π is defined as

161
$$\Pi(\sigma, \sigma') = \Pi(\tau, \tau') = \begin{cases} 1 & \text{if } \sigma \in \sigma' \text{ and } \tau \in \tau' \\ 0 & \text{otherwise.} \end{cases} \quad [3]$$

162 where $\sigma' = (\sigma \pm \Delta\sigma/2)$ and $\tau' = (\tau \pm \Delta\tau/2)$ and determines if a water parcel falls into a chosen σ - τ class. The volume integration
 163 was made in σ - τ classes with density intervals of 0.05 kg m^{-3} between 23 and 27.5 kg m^{-3} and spice intervals of 0.1 kg m^{-3}
 164 between 4 and 8.5 kg m^{-3} . This choice reflects a trade-off between adequately representing each water mass class and ensuring
 165 that the mode water layer is well resolved.

166 Using equation [1], a set of linear equations can be generated to equate the volume trend and the interior water-mass
 167 transformation in σ - τ coordinates as $dV/dt = \mathbf{Ax}$, where dV/dt is the observed change in volume of each sigma-spice class,
 168 divided by the relevant time interval; \mathbf{A} is the matrix of coefficients of the linear equations; and \mathbf{x} is the vector of the resulting
 169 diasurface transformations and exchange flux. This system is solved by means of a least squares regression for the unknown

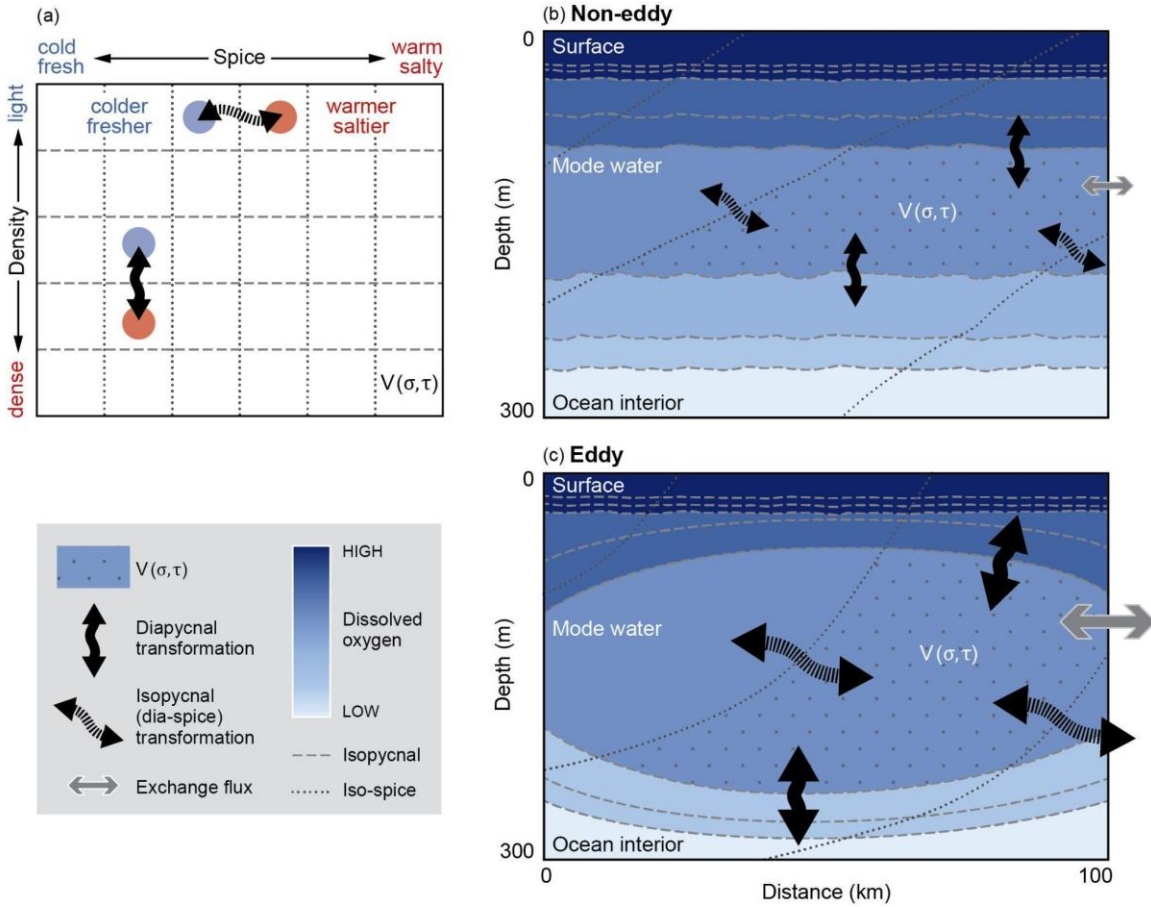
170 transformation and exchange flow. The detailed methodology can be found in the Supplementary Information. The solution \mathbf{x}
171 was then decomposed into the transformation across spice and density surfaces and the exchange flux across the geographical
172 domain.

173

174 The volume of water bounded by a given tracer iso-surface (e.g., here σ or τ) can change due to mixing across the tracer iso-
175 surface or due to volume transport into or out of the domain. However, it can also change by air-sea buoyancy fluxes if the
176 tracer surface outcrops at the ocean surface (Evans et al., 2014; 2023; Groeskamp et al., 2019). To assess the role of surface
177 forcing, we applied the water mass transformation framework in temperature-salinity (T-S) space (Evans et al., 2014; 2023).
178 Using glider and Argo T-S observations, together with ERA5 air-sea buoyancy fluxes (Hersbach et al., 2020), we diagnosed
179 the surface transformation of distinct T-S classes, thereby identifying which classes are actively transformed by air-sea fluxes.
180 These classes were mapped into σ - τ space and compared with the σ - τ domain of the mode water (Figure S2), showing no
181 overlap. The classes influenced by surface fluxes lie well above the density range of the mode water (Figure S2), indicating
182 that surface buoyancy forcing does not influence the observed mode water transformations. Moreover, we exclude a subduction
183 term through the base of the deepest mixed layer (in contrast to Portela et al. 2020b). This is justified because we start the
184 water-mass transformation analysis well after mode waters are capped and the σ - τ classes lie well below the surface mixed
185 layer under strong stratification ($O(10^{-3}) \text{ s}^{-2}$).

186

187 The water-mass transformation framework was applied to 20 repeated ocean glider sections, each 60 km long and extending
188 from the surface to 500 m depth, at the location indicated in black in Figure 1a. To minimize the influence of shelf processes
189 on the transformation, sections begin 10 km from the 300 m isobath, where depths exceed 500 m. The temporal resolution is
190 approximately 3 days between successive sections. The first transect included in the analysis starts on 25 March, roughly a
191 week after restratification, to minimize the influence of potential subduction/exchange with the surface mixed layer. Moreover,
192 the framework is also applied to the across-gulf monthly climatology to obtain a climatological average of water mass
193 transformations in the region. As restratification of the surface mixed layer typically completes by mid-March (Font et al.,
194 2022), we restrict the analysis of monthly transformations to the period from April onwards. The residual errors for both
195 datasets, computed as $|(dV/dt - \mathbf{Ax})|/|(dV/dt)|$, were on average of order 10^{-5} , which is on the higher end of values reported in
196 previous studies (e.g., Portela et al., 2020b).



197

198 **Figure 2. Water mass transformation framework for eddy and non-eddy sections.** (a) Diagram showing the effect of the transformation
199 of a given water class in $\sigma\tau$ space (adapted from Figure 1a from Portela et al. (2020b)), and (b-c) processes involved in the volume change
200 of a given $\sigma\tau$ class in geographical coordinates for (b) a non-eddy and (c) an eddy section colored by dissolved oxygen concentration.

201 **3. Results**

202 **3.1 Timescales of transformation of mode water**

203 We examine the seasonal-scale evolution of mode-water properties and transformations using the monthly Argo climatology
204 (April–June). This climatological view captures the broad, low-frequency changes as the mode water evolves through late
205 spring and early summer, but necessarily smooths over shorter-term variability. Mode water forms between February and
206 March, and lingers as a homogeneous layer below the seasonal pycnocline (Figure 1d-e), forming a boundary between the
207 mixed layer above and the Arabian Sea oxygen minimum zone below ($< 60 \mu\text{mol kg}^{-1}$) (Figure 1e). Climatologically, the low
208 stratification characteristic of mode water in the Sea of Oman is present until June (Figure 1d), but it can persist longer inside
209 eddies (Font et al. 2025; Liu et al., 2013). Over seasonal timescales, the transformation framework reveals a net shift toward
210 mintier (i.e., fresher and colder) and lighter waters, driven by negative isopycnal and diapycnal transformations (Figure 3).

211 Isopycnal transformation (Figure 3a) indicates mixing into colder, fresher classes, while diapycnal transformation (Figure 2c)
212 reflects mixing into lighter classes. On average, the isopycnal transformation dominates ($-0.015 \pm 0.009 \text{ m}^2 \text{ s}^{-1}$), with a
213 magnitude approximately three times larger than the diapycnal transformation ($-0.005 \pm 0.008 \text{ m}^2 \text{ s}^{-1}$) (Figure 3a, c, and f). The
214 signs of the transformation terms reflect the direction of the fluxes between density and spiciness classes, whereas the net $\Delta\sigma$ and
215 $\Delta\tau$ reflect the evolution of the volume-weighted mean properties. Thus, there is mode water volume formed due to
216 transformation from lighter and mintier waters (red shading, Figure 3b), but a large destruction predominantly in the lighter
217 and spicier classes of mode water (blue shading, Figure 3b). This fact, alongside a thinning of the mode water layer
218 ($\Delta\text{Thickness}=10 \text{ m month}^{-1}$; Figure 3d), results in mean mintification and densification of mode water between March and
219 June ($\Delta\tau = -0.03 \text{ kg m}^{-3} \text{ month}^{-1}$, $\Delta\sigma = 0.0013 \text{ kg m}^{-3} \text{ month}^{-1}$, Figure 3e).

220
221 The previous analysis was based on monthly climatologies and, therefore, mesoscale and smaller scale contributions to the
222 transformation are largely averaged out. In contrast to the climatological perspective, the high-resolution glider time series
223 resolves submonthly variability and therefore reveals the episodic, intraseasonal changes in mode water structure and
224 transformations that are absent from the monthly climatology. This allows us to directly quantify short-lived events associated
225 with transient processes, such as mesoscale eddies. Over shorter timescales, the high-resolution time series provided by the
226 ocean gliders offers a unique view that highlights the large variability of mode water thickness and depth due to eddy presence
227 and topographical interactions with the shelf break (Figures 1e and 3d). We observe a transition toward mintier waters
228 throughout the study period ($\Delta\tau = -0.04 \text{ kg m}^{-3} \text{ month}^{-1}$), albeit with notable temporal variability as indicated by the sign
229 changes in the isopycnal transformation (Figure 3ef). Until early April, waters become spicier (isopycnal transf. > 0). Then,
230 they shift to mintier conditions (isopycnal transf. < 0), which last until the end of April. After that, waters get spicier again.
231 This behaviour reverses in mid-May, and the period ends with mintier waters (isopycnal transf. < 0). A similar pattern is
232 observed in the diapycnal transformation. Over the sampled period, waters get slightly lighter ($\Delta\sigma=0.001 \text{ kg m}^{-3} \text{ month}^{-1}$) but
233 with large variability ($\Delta\sigma = \pm 0.02 \text{ kg m}^{-3}$; Figure 3e). Densification occurs until early April (diapycnal transf. > 0), followed
234 by a period of lightening (diapycnal transf. < 0), and a shift to densification after mid-May (diapycnal transf. > 0 ; Figure 3e).
235 Notably, the isopycnal and diapycnal transformations are well correlated through most of the period until they begin to diverge
236 in late April, when the isopycnal transformation changes sign approximately two weeks before the diapycnal transformation
237 (Figure 3f).

238
239 Despite the variability, the mean magnitude of the glider-based transformations is of the same order ($10^{-2}\text{--}10^{-3} \text{ m}^2 \text{ s}^{-1}$) as the
240 climatological transformation, with twice the contribution from isopycnal to diapycnal transformation, yet larger extremes for
241 the latter (isopycnal: $-0.004 \pm 0.027 \text{ m}^2 \text{ s}^{-1}$; diapycnal: $0.002 \pm 0.029 \text{ m}^2 \text{ s}^{-1}$; Figure 3f). We suggest that the high variability in
242 both positive and negative diapycnal transformations is averaged out in the monthly climatological sections.

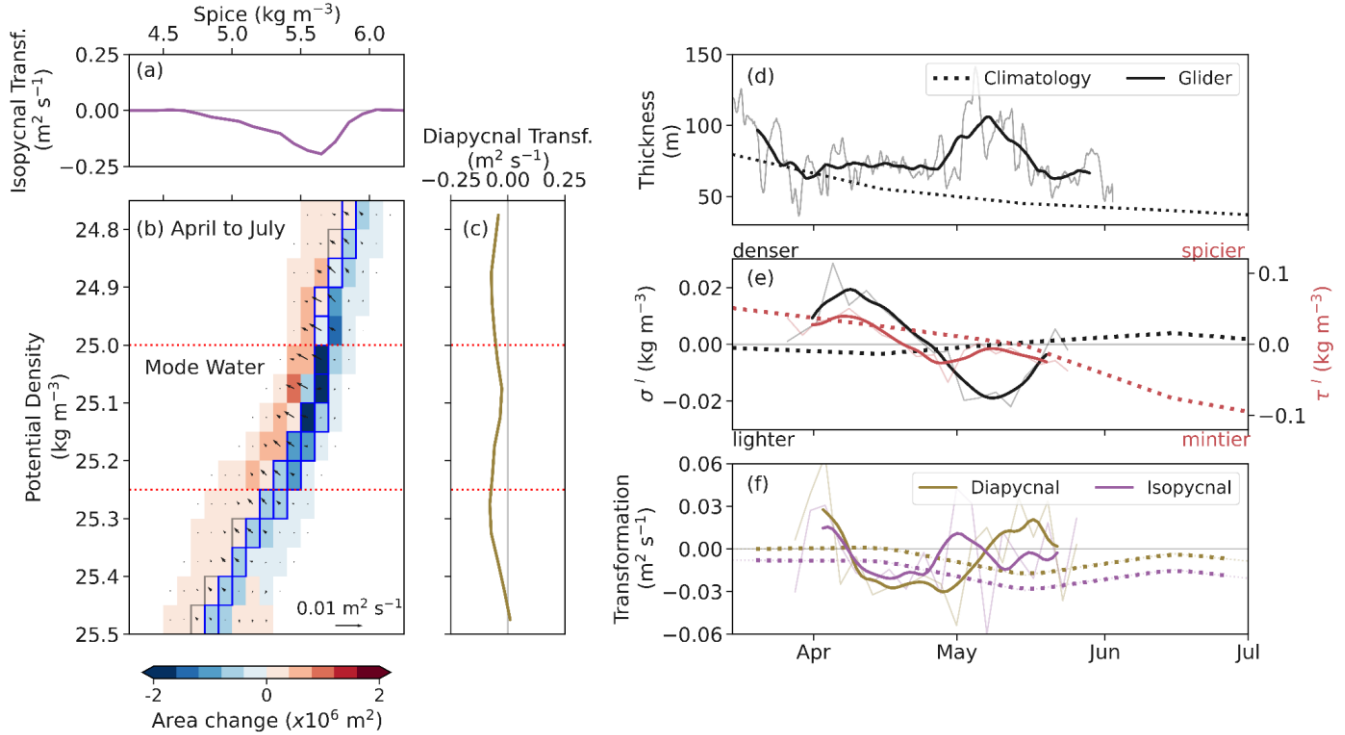
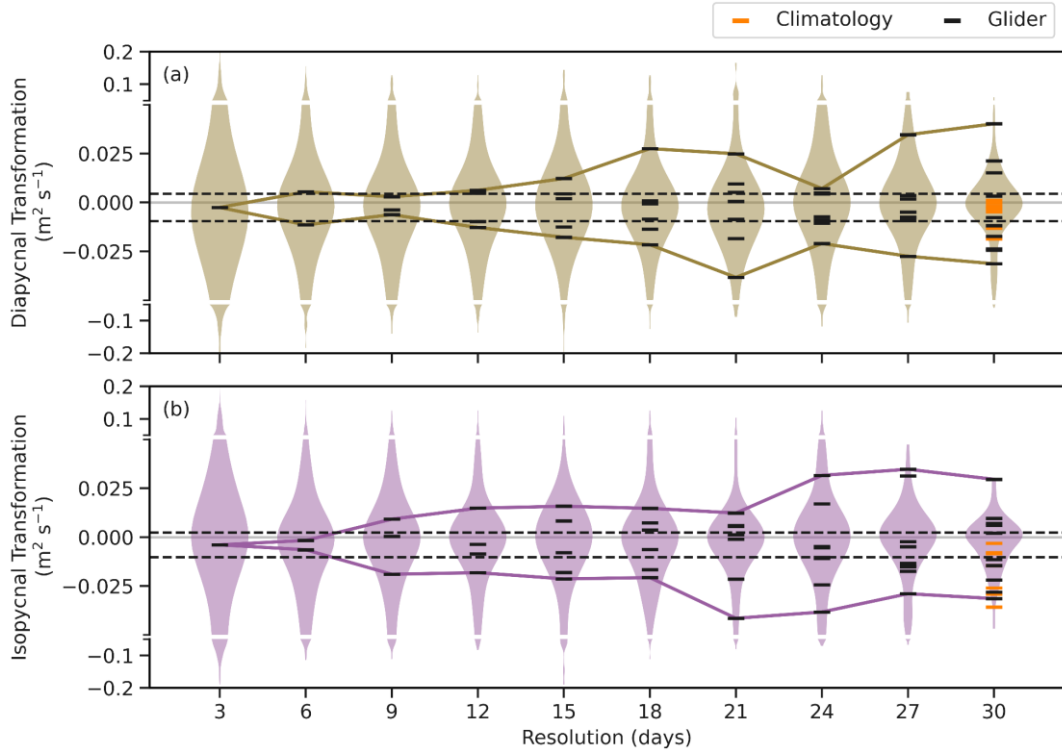


Figure 3: Timescales of mode water transformation. (a) Integrated isopycnal transformation per spice class from panel (b). (b) Climatological area changes between April and June. Arrows depict the transformation direction and magnitude per σ - τ water class. Mode water band (σ : 25–25.25 kg m^{-3}) is delimited between the horizontal red dotted lines in panels (b) and (c). The σ - τ classes at the domain's boundary, thus, subjected to exchange flux, are marked with squares, colored blue when contributing more than 25% of the area loss, and red when contributing more than 25% of the area gain. (c) Integrated diapycnal transformation per potential density class from panel (b). (d) Mode Water thickness from glider data (solid gray), after applying a 24-hour rolling mean (solid black), and the climatology (dotted). (e) Temporal anomalies of potential density (σ') and spice (τ') computed as deviations from their time-mean over the March–July period as $\sigma'(t)=\sigma(t)-\bar{\sigma}$ and $\tau'(t)=\tau(t)-\bar{\tau}$ where $\bar{\sigma}$ and $\bar{\tau}$ are the time-means computed over the analysis period. Solid light lines show the 3-day glider anomalies; solid dark lines show the glider anomalies after applying a 10-day rolling mean; dotted lines show the monthly climatological anomalies. (f) Integrated diapycnal transformation (brown) and isopycnal transformation (purple) for mode water (σ : 25–25.25 kg m^{-3}), from glider data (solid light), the glider after applying a 10-day rolling mean (solid), and the climatology (dotted).

Applying the water-mass transformation framework to high-resolution glider sections enables quantification of transformation variability across different temporal resolutions and scales. To assess how sampling period and resolution affect the ability to reproduce the high-resolution glider mean, the 3-day transformation time series (Figure 3f) was sub-sampled over a continuous range of intervals from 3-day to monthly (Figure 4, scatters). For each interval, we generated multiple realizations of a mean by shifting the starting time iteratively by 3-day steps —for example, a 6-day sampling interval yielded two mean estimates, while a 30-day interval produced 10. This approach provides a distribution of possible means for each effective sampling resolution. To illustrate how smoothing influences variability, we also applied rolling means of increasing window length to the 3-day series (shown as violin plots in Figure 4). As the window size increases, extreme values in both isopycnal and diapycnal transformation are progressively damped (Figure 4). The spread in the mean transformation (black markers)

increases as resolution decreases (up to monthly climatology resolution, orange markers). This spread reflects the reduced likelihood of recovering the 3-day mean. If each transformation were insensitive to the sampling frequency, its magnitude would remain close to the high-resolution mean regardless of the sampling period. From an Argo monthly climatological perspective, the probability of recovering the 3-day sampled mean within one standard error is about 60% for the diapycnal transformation and 40% for the isopycnal transformation. Using the glider sub-sampled timeseries, this likelihood drops with coarser sampling: from 75% at 6-day intervals to less than 50% at sampling frequencies longer than 12 days. These results highlight the importance of collecting data at least weekly to capture the influence of high-frequency variability. For example, sampling only once every 30 days reduces the chance of capturing the 3-day mean by about 85% compared to 3-day sampling.



276

Figure 4. Sensitivity of mean transformation estimates to sampling resolution. (a) Diapycnal and (b) isopycnal transformations distribution after smoothing the transformation with a resolution-day rolling mean as violin plots. Lines (-) indicate mean transformations estimated from sub-sampling the 3-day time series at coarser intervals (resolutions): black for the glider dataset, and orange for the climatological dataset. The coloured line envelopes the minimum and maximum mean transformations from sub-sampling the time series, and the black dashed lines indicate the transformations within the mean ± 1 standard error of the highest resolution (3-day).

282

283 3.2 Enhancement of diapycnal and isopycnal transformation by mesoscale eddies

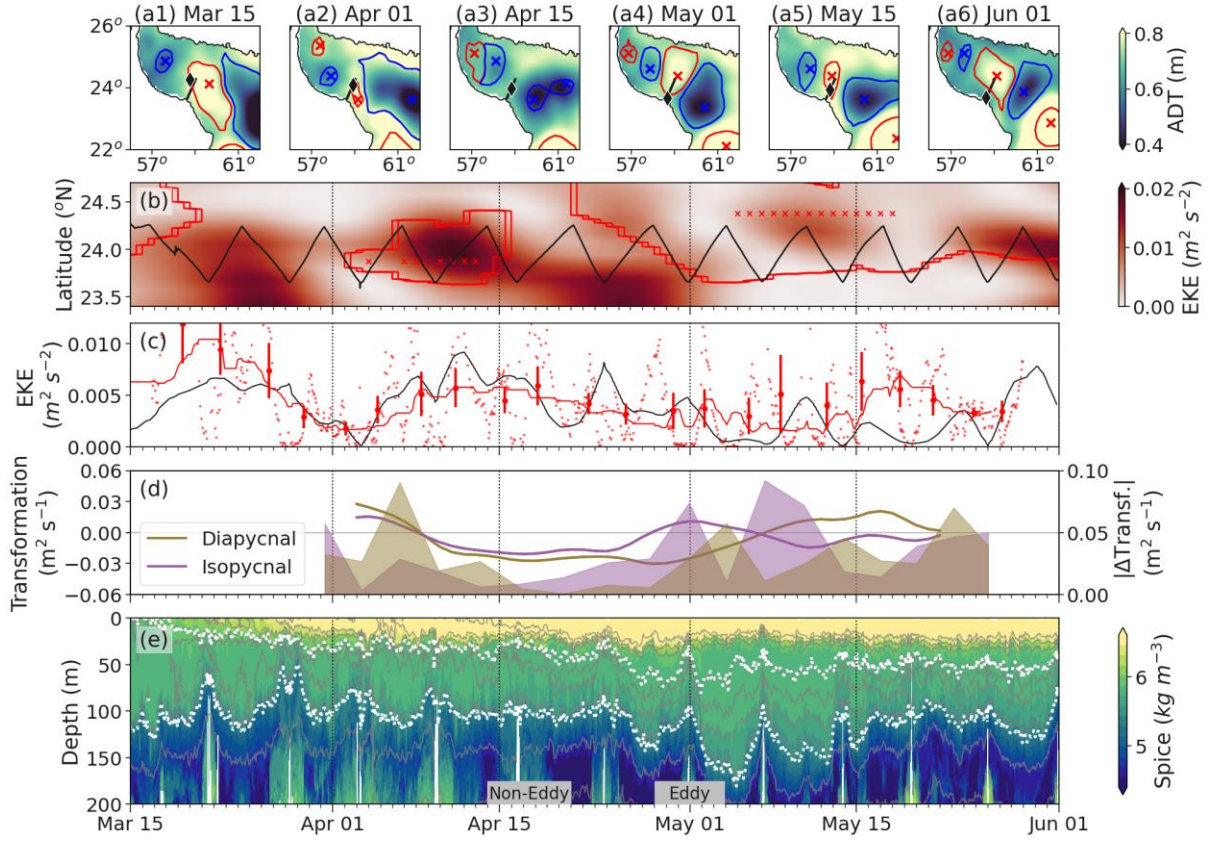
284 The high-resolution observations provide an excellent dataset to analyze the temporal and spatial evolution of mesoscale eddy
285 activity and associated water mass transformation within the mode water from mid-March to early June. The ToEddies Global

286 Mesoscale Eddy Atlas (see Section 2.1, Laxenaire et al., 2024) reveals the presence and persistence of anticyclonic and
287 cyclonic eddies in the Sea of Oman during this period (Figure 5a), as well as the crossing of three anticyclones along the
288 glider's trajectory (Figure 5b). These mesoscale structures dominate the surface circulation during the sampling period and
289 undergo gradual displacement and structural changes over time. The glider's path through these eddies (Figure 5b) captures
290 the dynamic interaction between the platform and the evolving eddy field. Enhanced EKE values (Figure 5c) correspond to
291 periods of intensified mesoscale activity and potential eddy-glider encounters. The agreement between the satellite-derived
292 EKE and the glider-derived EKE confirms the presence of high-EKE periods during the campaign.

293 The glider-derived observations reveal the vertical imprint of these eddies on the thermohaline structure and associated water
294 mass transformation. The observed vertical displacements of isopycnals and intrusions of anomalous water masses (Figure 5e)
295 are consistent with mesoscale stirring. These anomalies coincide with changes in isopycnal and diapycnal transformation along
296 with mesoscale eddy activity (Figure 5d), suggesting an active role of mesoscale dynamics in modulating vertical exchanges
297 and interior ventilation. For instance, around April 6, when an anticyclone is present, a marked increase in surface EKE (Figure
298 5b) corresponds with simultaneous peaks in both isopycnal and diapycnal transformation rates of change ($|\Delta Transf.|$; Figure
299 5c and d), suggesting intensified stirring and mixing as the glider samples through the eddy structure.

300 Around April 15 (Non-eddy case), the mesoscale eddy moves away from the glider transect, as indicated by both the ADT
301 maps (Figure 5a3) and the glider spice time series, where isopycnals flatten (Figure 5e). The glider trajectory during this period
302 does not intersect any prominent eddy (Figure 5b), suggesting that it is transiting through a relatively quiescent background
303 flow. Correspondingly, the transformation rates, both diapycnal and isopycnal, are stable and similar to the ones derived from
304 the climatology (negative and $O(10^{-2})$, Figure 3f and 5d). This calm period contrasts with the more dynamic intervals before
305 and after, suggesting that enhanced transformation is closely tied to eddy presence and activity. The transformation around
306 April 15 thus serves as an ad hoc baseline, highlighting the mesoscale-driven nature of the stronger exchange events observed
307 throughout the record.

308 A second event occurs around April 27-May 3 (Eddy case), when the glider crosses an anticyclone again (Figure 5a4, b, and
309 e) and isopycnal transformation increases (Figure 5d), underscoring the dominant role of mesoscale processes in lateral tracer
310 transport. This is followed by a pronounced diapycnal transformation event, likely driven by vertical exchanges at eddy
311 boundaries and/or interaction with shelf bathymetry.



312

313 **Figure 5. Mesoscale eddies and mode water transformation.** (a1-a6) Snapshots of Absolute Dynamic Topography (ADT) in the Sea of
 314 Oman on the 1st and 15th day of each month between March and June. The glider location on each date is marked with a black diamond,
 315 and its transect is shown as a black line. The eddies are retrieved from TOEddies Atlas (anticyclones in red, cyclones in blue): the
 316 eddy center (x) and the maximum extent (solid contour) are also shown. (b) Hovmoller of EKE from satellite-derived geostrophic velocities with
 317 the glider track in black. The eddy center (x) and the contours of maximum extent (solid contour) are shown as in panel (a). (c) EKE retrieved
 318 from the glider dive-average current (small red dots), after applying a 24-hour rolling mean (red line), and average per transect (large red
 319 dots) with the standard deviation for the transect as a vertical red line. EKE retrieved from ADT (black line), scaled by a factor of 2 to match
 320 the magnitude of the EKE from the glider. (d) Mean transformation per transect (left axis), and the absolute change of transformation over
 321 time ($|\Delta\text{Transf.}|$; right axis) to show when the change in transformation occurs for both diapycnal and isopycnal transformation. (e) Spice
 322 time series with the top and bottom boundaries of the core of the mode water ($25-25.25 \text{ kg m}^{-3}$; white dotted lines) and isopycnals (gray
 323 lines). The two labels show the periods chosen as “Eddy” and “Non-Eddy” study cases in Figure 6.

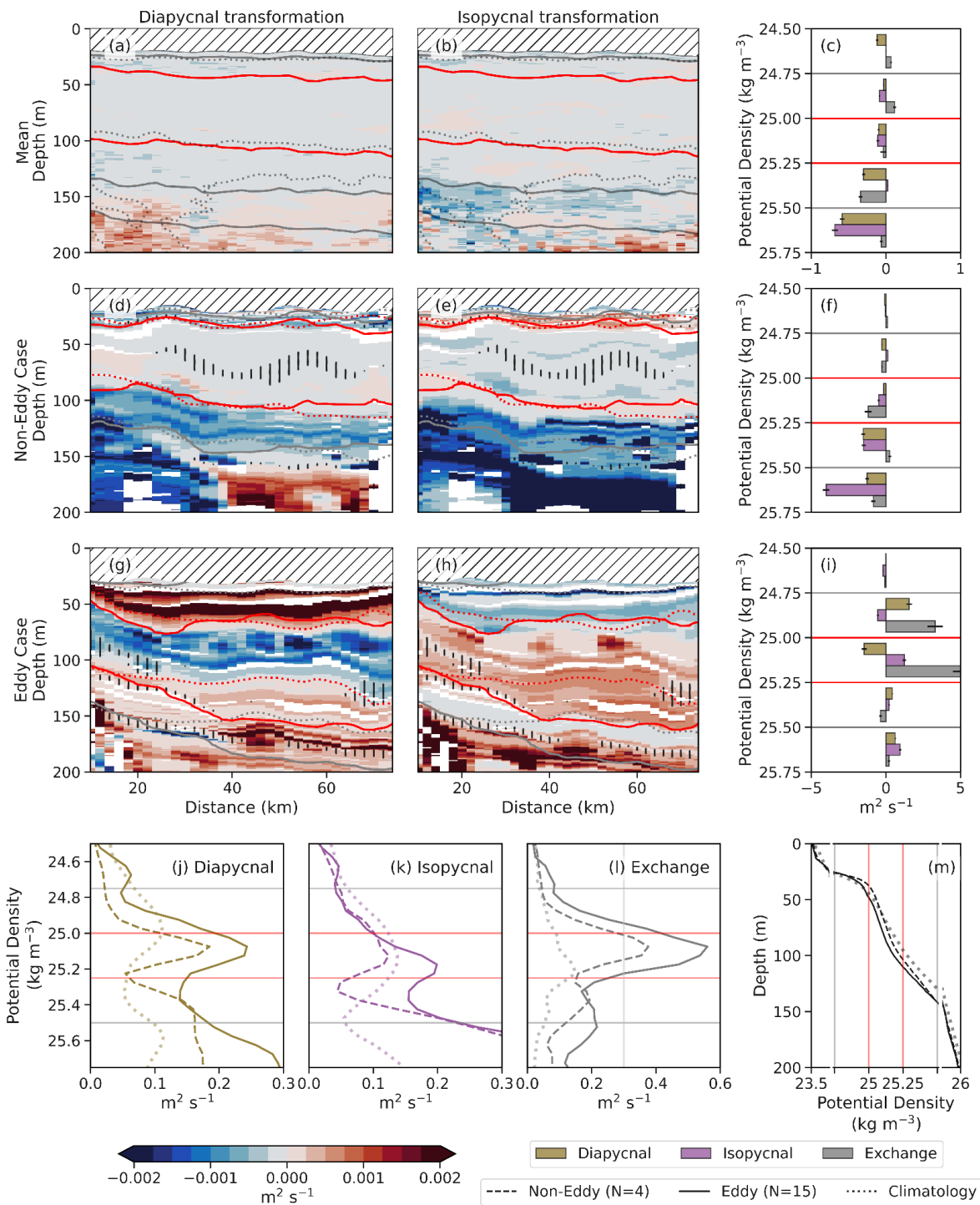
324 To investigate the spatial structure of water-mass transformation and its dependence on mesoscale eddy activity, we remapped
 325 the transformations in distance-pressure coordinates from the shelf. The transformation rates, when averaged over the repeated
 326 sections of the entire glider deployment (Figure 6a-b) show weak diapycnal and isopycnal transformations. This mean view
 327 closely resembles those derived from the monthly climatological dataset, despite the climatology being composed of basin-

328 wide Argo profiles (Figure 3b), reaffirming that glider-based observations can reproduce the climatological view when
329 averaged over long enough timescales, and that high-frequency variability is largely smoothed out in monthly means.

330 We compare the average transformation sections with two contrasting case studies: one with no eddy presence (Figure 6d-f)
331 and one with an eddy (Figure 6g-i; the periods marked in Figure 5e). The Non-Eddy Case (Figure 6d-f) provides a baseline
332 scenario where the glider transect occurs in a region with no identifiable eddy, as confirmed by the lack of coherent structures
333 in the ADT maps (Figure 5a.3). Both isopycnal and diapycnal transformation rates are comparable to the climatological mean
334 and are relatively weak within the mode water core (~ -0.01 and $0.005 \text{ m}^2 \text{ s}^{-1}$, respectively; Figure 3 and 6d-e).

335 The Eddy case (Figure 6g-i) captures a glider transect through an anticyclonic eddy. In contrast to the quiescent background
336 conditions seen in the Non-Eddy Case, this eddy drives an order of magnitude enhancement of diapycnal transformation above
337 and below the mode water core ($\sim 0.05 \text{ m}^2 \text{ s}^{-1}$), pointing to intense vertical exchanges associated with eddy-induced mixing.
338 Isopycnal transformation is also intensified and spatially coherent along sloping density surfaces ($\sim 0.04 \text{ m}^2 \text{ s}^{-1}$). The elevated
339 isopycnal transformation rates imply vigorous lateral mixing along density surfaces, enhanced by eddy-driven stirring and
340 frontal slumping. Such strong transformation rates suggest that the eddy acts as an efficient conduit for water-mass
341 transformation, especially within mode water density layers. This case highlights the dynamically active role of anticyclonic
342 eddies in modulating both vertical and lateral mixing processes, and thus promoting the redistribution of heat and salt and
343 contributing to the ventilation of the ocean interior.

344 The exchange term (grey bars in Figure 6c, f, and i), calculated as the residual in the transformation budget, serves as a proxy
345 for advective fluxes through the section and can highlight dynamically active regions where advection dominates over mixing.
346 In the Eddy Case, this term is particularly pronounced, indicating a strong advective component related to eddy presence (0.59
347 $\pm 0.48 \text{ m}^2 \text{ s}^{-1}$; Figure 6i). In contrast, the exchange flux is much weaker in both the mean section and the Non-Eddy Case (0.16
348 $\pm 0.13 \text{ m}^2 \text{ s}^{-1}$; Figure 6c and f), suggesting a reduced role of advective processes. Eddies, both surface and subsurface, are well
349 known to transport coherent parcels across long distances (e.g, Frenger et al. 2018), driving the strong exchange seen here.
350 Altogether, the exchange term adds an important dimension to the volume budget, helping to quantify the net effect of non-
351 mixing processes, and further supporting the view that mesoscale advection can be a dominant pathway for ventilation and
352 altering stratification in the upper ocean.



353

354

355

Figure 6. Case studies. (a) Mean diapycnal and (b) isopycnal transformations in geographical space (distance from shelf vs. depth). Gray lines: isopycnals; red lines: 25.00 and 25.25 kg m^{-3} ; dotted: iso-salinity. Density classes lighter than 24.5 kg m^{-3} are diagonally hatched (//) to

356 exclude water classes with a potential air-sea flux transformation term. (c) Diapycnal, isopycnal transformations, and exchange fluxes
357 averaged over 0.25 kg m^{-3} density bands. Panels (d-f) show a case without an eddy (Non-Eddy Case); (g-i) a case with an eddy (Eddy Case).
358 (d, g) Diapycnal, (e, h) isopycnal transformations in geographical space; (f, i) transformations and fluxes in density space. In (d-e, g-h),
359 dotted and solid isopycnals correspond to initial and final time steps. Vertical hatches (||) mark regions where exchange flux accounts for >
360 25% of volume change. Density classes lighter than 24.5 kg m^{-3} are hatched (//) to exclude water classes with a potential air-sea flux
361 transformation term. (j-l) Spice-integrated averages of (j) diapycnal, (k) isopycnal transformations, (l) exchange flux; lines: eddy (solid),
362 non-eddy (dashed), and Argo climatology (dotted). The averages are on the absolute values of the transformations, thus focusing on their
363 magnitudes rather than their direction. (m) Mean density profile for eddy (solid) and non-eddy (dashed) classification, and climatology
364 (dotted). N indicates the number of glider sections that contribute to the mean. Lines in (c, f, i, j-l) separate 0.25 kg m^{-3} bands; red lines
365 denote the potential density range of mode water (25 and 25.25 kg m^{-3}). Note differing x-axis ranges in (c, f, i) and (j-l).

366 The impact of the dynamical regime on transformation magnitudes within the mode water layer is striking (Figure 6j-l). The
367 passage of mesoscale eddies leads to a marked intensification of all three components of the volume budget within the mode
368 water layer, reflecting enhanced isopycnal and diapycnal mixing as well as increased advective exchange (see summary
369 schematic in Figure 2). Compared to non-eddy conditions, diapycnal, isopycnal, and exchange fluxes increase by 61%, 45%,
370 and 66%, respectively (Figure 6j-l). In the absence of eddies, mode water undergoes significantly weaker transformation - with
371 transformation magnitudes similar to the climatological average (Figure 6j-l). It is noteworthy that these estimates represent
372 integrated values across the glider transect, and local transformation rates may vary substantially, enhanced or suppressed,
373 depending on eddy position, intensity, and interactions with topography.

374 To further contextualize these differences, we compared the transformation rates under eddy and non-eddy conditions with the
375 climatological mean derived from Argo profiles. Diapycnal transformation exhibits the largest relative increase during eddy
376 periods, rising by 163% compared to the climatological mean (Figure 6j). This substantial enhancement likely reflects
377 intensified vertical exchange driven by eddy-related processes that are absent from monthly climatologies. Even outside of
378 eddy influence, the diapycnal transformation from the glider data remains elevated ($\sim 0.13 \text{ m}^2 \text{ s}^{-1}$, a 63% increase relative to
379 the climatological mean), likely due to the glider's ability to resolve finer-scale vertical structure and fluxes resulting from
380 diapycnal mixing.

381 Isopycnal transformation also increases under eddy influence, with a pronounced peak in the mode water layer ($\sim 0.16 \text{ m}^2 \text{ s}^{-1}$),
382 corresponding to a 43% rise over the climatological mean (Figure 6k). This points to enhanced lateral stirring and strain-driven
383 intrusions along density surfaces, characteristic of mesoscale eddy activity. In contrast, during non-eddy conditions, isopycnal
384 transformation remains weaker and closely matches the climatological estimate ($\sim 0.11 \text{ m}^2 \text{ s}^{-1}$). This suggests that eddy-related
385 strain and intrusions play a major role in redistributing water masses and altering thermohaline structure within the mode
386 water. In the absence of eddies, isopycnal transformation is reduced and comparable to the climatological mean.

387 The exchange component (Figure 6l) similarly shows a pronounced peak in the presence of eddies ($\sim 0.5 \text{ m}^2 \text{ s}^{-1}$, 140% increase
388 relative to climatology), and is notably lower under non-eddy conditions ($\sim 0.3 \text{ m}^2 \text{ s}^{-1}$, 45% above the climatological mean).
389 The greater exchange fluxes observed in the high-resolution glider dataset reflect the contribution of strong mesoscale
390 advection not captured in the monthly climatologies.

391 **4. Discussion**

392 Mode waters play a crucial role as pathways connecting the surface and subsurface ocean, influencing the distribution and
393 transport of tracers, including heat, salt, oxygen, and other biogeochemical properties. For instance, in the Arabian Sea, mode
394 waters bound the upper oxycline of the Arabian Sea oxygen minimum zone, thus playing a central role in shaping regional
395 oxygen distributions (Font et al., 2025). As shown by Jutras et al. (2025), at long-term and large spatial scales, more than 50%
396 of oxygen changes along mode water ventilation pathways can be attributed to mixing with surrounding oxygen-poorer waters.
397 While we do not diagnose oxygen directly, our results extend this understanding by showing that the physical drivers of such
398 mixing are strongly intensified at short timescales during eddy activity. These episodic but vigorous transformation events
399 likely modulate ventilation efficiency and tracer redistribution within mode waters.

400 High-resolution glider observations reveal the much greater intermittency and intensity of transformation processes missed in
401 climatological datasets. This challenges the underlying assumptions of climatological approaches for estimating water mass
402 transformation and understanding upper-ocean dynamics. Monthly climatologies, while valuable for capturing broad seasonal
403 trends, inherently smooth out the episodic and spatially localized processes (e.g., mesoscale eddies and submesoscale fronts)
404 that strongly contribute to net water-mass transformation. Our analysis shows that a significant fraction of the total
405 transformation, particularly within the mode water layer, occurs during short-lived eddy events, which are effectively diluted
406 in monthly-averaged fields (Figures 3 and 4). As a result, climatological approaches miss sub-monthly variability and
407 underestimate both the intensity and variability of transformation processes (Figure 4), particularly the contributions from
408 isopycnal stirring and advective exchange (Figure 6).

409 Mesoscale eddies can trap and transport mode water, preserving its properties and prolonging the lifespan of this buffer layer.
410 In the Arabian Sea, eddies have been shown to modulate the distribution and characteristics of water masses such as the
411 Arabian Sea High Salinity Water (Thoppil, 2024; Trott et al., 2019). Moreover, anticyclonic eddies have been found to trap
412 more mode water than cyclonic ones (e.g., Liu et al., 2013 in the North Atlantic), contributing significantly to total mode water
413 transport—up to 17% south of the Kuroshio Extension (Shi et al., 2018), comparable to the transport by the mean flow (Xu et
414 al., 2016). We complement these findings by showing that, at short spatial and temporal scales, eddies transform mode waters
415 (Figures 2 and 5-6). We hypothesize that by driving intermittent but intense exchanges, eddies can influence stratification and
416 shape mode water transformation. While the water-mass transformation framework allows for indirect estimation of the
417 integrated effects of mixing, understanding the specific mechanisms behind these transformations, particularly at fine scales,

418 requires direct observations. Including turbulence measurements, such as microstructure-derived diffusivities to resolve the
419 role of vertical mixing, could allow for disentangling those from lateral stirring and advection, and thus refine the interpretation
420 of transformation processes in dynamic regions like the Sea of Oman.

421 Mesoscale eddies play a crucial role as biogeochemical agents. Subsurface eddies can carry oxygen and nutrient signatures
422 over distances of hundreds of kilometers (Frenger et al., 2018) and can influence subsurface biogeochemistry over extended
423 periods (Karstensen et al., 2017; Schütte et al., 2016). Mesoscale eddies influence the boundaries of oxygen minimum zones
424 (e.g., Auger et al., 2021; Eddebar et al., 2021; Sarma et al., 2018), and it has been shown that eddy-resolving models lead to
425 better representation of these zones' intensity and extent (Calil, 2023; Lévy et al., 2022; Resplandy et al., 2012). The intensified
426 isopycnal and exchange-driven transformations we observe during eddy periods (Figures 2 and 5-6) imply stronger horizontal
427 and vertical transport, reinforcing the idea that they play a disproportionate role in regulating fluxes of heat, salt, and
428 biogeochemical tracers in the upper ocean.

429 We suggest that ventilation timescales for the mode water layer are highly variable in time and space. This variability has
430 significant implications for interpreting biogeochemical observations or budgets derived from time-averaged or coarse-
431 resolution data, which may underestimate the influence of short-lived but intense eddy events. Our findings raise important
432 questions about the timescales over which biological activity and physical mixing interact and balance across broader spatial
433 and temporal domains, which need to be further investigated. Capturing this level of detail is essential for improving
434 biogeochemical model parameterizations, which rely on an accurate representation of exchange rates and timescales.
435 Moreover, it provides a basis for evaluating how these processes may respond to future changes in ocean stratification, eddy
436 activity, and circulation patterns.

437 **5. Conclusion**

438 Through a detailed characterization of the temporal variability, we find that the mode water core in the Sea of Oman becomes
439 progressively denser and mintier as its volume diminishes between March (when it is capped just below the surface) and June.
440 By applying the water mass transformation framework in σ - τ space to both high-resolution glider data and a monthly
441 climatological Argo dataset, we quantify the dominant timescales and transformation processes acting within the mode water
442 layer. Isopycnal transformation rates were, on average, three times greater than diapycnal transformation. However, episodic
443 mesoscale eddy events lead to locally enhanced diapycnal fluxes.

444 This framework, traditionally applied to coarse-resolution climatologies or model simulations, proves capable of capturing
445 transformation variability and extremes that are absent from monthly climatological datasets, highlighting the unique value of
446 gliders. We estimate that the likelihood of recovering the 3-day sampled mean from monthly climatologies is between 40-
447 60%, emphasizing how coarse temporal sampling can distort our understanding of the inherently episodic and dynamic nature
448 of water-mass transformation. This observed variability is attributed to mesoscale eddies.

449 During eddy passages, all three components of the mode water volume budget -diapycnal, isopycnal transformations, and
450 exchange flux- are significantly intensified compared to non-eddy conditions (as the schematic in Figure 2 shows). Overall,
451 our results demonstrate that transformation within the mode water layer is strongly enhanced by mesoscale activity. These
452 findings underscore the need for sustained, high-resolution observations, as they would allow us to link integrated
453 transformation rates more explicitly to underlying physical drivers, resolve the vertical structure of mixing processes, and
454 assess the role of mesoscale and submesoscale dynamics and topographic interactions. Ultimately, combining transformation
455 diagnostics with targeted in situ measurements will improve our ability to constrain ocean ventilation and tracer budgets, refine
456 model parameterizations, and evaluate how these processes respond to a changing climate.

457 **Code availability.** The software associated with this paper is publicly available on GitHub
458 (https://github.com/EstelFont/Transforamtion_Mode_Water).

459 **Data availability.** The Argo data used in this study is available by the International Argo Program and the national programs
460 contributing to it for the domain 22.5-26 °N, 56-61°E and between 2000-2023 (Argo, 2023). Ocean glider data are available
461 from the British Oceanographic Data Centre (Queste et al., 2018b). The TOEddies can be accessed at SEANOE
462 (<https://doi.org/10.17882/102877>, Laxenaire et al., 2024). The bathymetry data are available from the GEBCO Compilation
463 Group (<https://doi.org/10.5285/f98b053b-0cbc-6c23-e053-6c86abc0af7b>, GEBCO, 2023). The sea surface geostrophic
464 velocities and absolute dynamic topography data are available from the E.U. Copernicus Marine Service Information
465 (<https://doi.org/10.48670/moi-00148>, CMEMS, 2025).

466 **Author contribution:** EF, EP, BYQ, and SS conceptualized the study. EF performed the data curation and formal analysis
467 and wrote the manuscript draft with input from MP. EP, BYQ, SS, and MP reviewed and edited the manuscript.

468 **Competing interests:** The authors declare that they have no conflict of interest.

469 **Acknowledgements:** We are grateful to the UEA Seaglider Facility, Sultan Qaboos University technical staff, and Five Oceans
470 Environmental Services consultancy for their technical help with fieldwork. We thank Lionel Guez for his assistance with
471 TOEddies detection and tracking, including help with data access and guidance on its use. We thank Gwyn Evans for the
472 publicly available water mass transformation framework code (<https://github.com/dgwynevans/wmt>), from which we adapted
473 our implementation.

474 **Financial Support:** EF and BYQ are supported by ONR GLOBAL Grant N62909-21-1-2008; MP and BYQ are supported by
475 Formas Grant 2022-01536. EF and SS are supported by a Wallenberg Academy Fellowship (WAF, 2015.0186) and by the
476 Swedish Research Council (VR, 2019-04400). S.S. has received co-funding from the European Union's Horizon Europe ERC

477 Synergy Grant programme under grant agreement No 101118693 - WHIRLS. Views and opinions expressed are however
478 those of the author(s) only and do not necessarily reflect those of the European Union or European Research Council Executive
479 Agency. Neither the European Union nor the granting authority can be held responsible for them. EF gratefully acknowledges
480 Adleberska Stiftelsen for partially funding a research visit to EP. Data collection was originally supported by the ONR
481 GLOBAL grants N62909-14-1-N224/SQU, Sultan Qaboos University grants EG/AGR/FISH/14/01 and IG/AGR/FISH/17/01,
482 and UK NERC grants NE/M005801/1 and NE/N012658/1.

483 **References**

484 Argo. (2023). Argo float data and metadata from Global Data Assembly Centre (Argo GDAC). [Dataset]. SEANOE.
485 <https://doi.org/10.17882/42182>

486 Auger, P. A., Bento, J. P., Hormazabal, S., Morales, C. E., and Bustamante, A.: Mesoscale variability in the boundaries of the
487 oxygen minimum zone in the eastern South Pacific: Influence of intrathermocline eddies, *J. Geophys. Res.-Oceans*, 126,
488 e2019JC015272. <https://doi.org/10.1029/2019JC015272>, 2021.

489 Badin, G., Williams, R. G., Jing, Z., and Wu, L.: Water mass transformations in the Southern Ocean diagnosed from
490 observations: Contrasting effects of air-sea fluxes and diapycnal mixing, *J. Phys. Oceanogr.*, 43, 1472–1484,
491 <https://doi.org/10.1175/JPO-D-12-0216.1>, 2013.

492 Calil, P. H. R.: High-resolution, basin-scale simulations reveal the impact of intermediate zonal jets on the Atlantic oxygen
493 minimum zones. *J. Adv. Model Earth Sys.*, 15, e2022MS003158. <https://doi.org/10.1029/2022MS003158>, 2023.

494 Donners, J., Drijfhout, S. S., and Hazeleger, W.: Water mass transformation and subduction in the South Atlantic, *J. Phys.*
495 *Oceanogr.*, 35, 1841–1860, <https://doi.org/10.1175/JPO2782.1>, 2005.

496 Eddebar, Y. A., Subramanian, A. C., Whitt, D. B., Long, M. C., Verdy, A., Mazloff, M. R., and Merrifield, M. A.: Seasonal
497 modulation of dissolved oxygen in the equatorial Pacific by tropical instability vortices, *J. Geophys. Res.-Oceans*, 126,
498 e2021JC017567, <https://doi.org/10.1029/2021JC017567>, 2021.

499 E.U. Copernicus Marine Service Information (CMEMS): Global Ocean Gridded L4 Sea Surface Heights and Derived
500 Variables Reprocessed 1993–ongoing, Marine Data Store (MDS) [data set], <https://doi.org/10.48670/moi-00148>, last access:
501 11 July 2025.

502 Evans, D. G., Zika, J. D., Naveira Garabato, A. C., and Nurser, A. J. G.: The imprint of Southern Ocean overturning on seasonal
503 water mass variability in Drake Passage, *J. Geophys. Res.-Oceans*, 119, 7987–8010, <https://doi.org/10.1002/2014JC010097>,
504 2014.

505 Evans, D. G., Holliday, N. P., Bacon, S., and Le Bras, I.: Mixing and air-sea buoyancy fluxes set the time-mean overturning
506 circulation in the subpolar North Atlantic and Nordic Seas, *Ocean Sci.*, 19, 745–768, <https://doi.org/10.5194/os-19-745-2023>,
507 2023.

508 Feucher, C., Portela, E., Kolodziejczyk, N., Desbruyères, D., and Thierry, V.: Subpolar gyre decadal variability explains the
509 recent oxygenation in the Irminger Sea, *Commun. Earth Environ.*, 3, 279, <https://doi.org/10.1038/s43247-022-00570-y>, 2022.

510 Font, E., Queste, B. Y., and Swart, S.: Seasonal to intraseasonal variability of the upper ocean mixed layer in the Gulf of Oman,
511 *J. Geophys. Res.-Oceans*, 127, e2021JC018045, <https://doi.org/10.1029/2021JC018045>, 2022.

512 Font, E., Swart, S., Vinayachandran, P. N., and Queste, B. Y.: On mode water formation and erosion in the Arabian Sea:
513 forcing mechanisms, regionality, and seasonality, *Ocean Sci.*, 21, 1349–1368, <https://doi.org/10.5194/os-21-1349-2025>, 2025.

514 Frajka-Williams, E., Eriksen, C. C., Rhines, P. B., and Harcourt, R. R.: Determining vertical water velocities from Seaglider,
515 *J. Atmos. Oceanic Technol.*, 28, 1641–1656, <https://doi.org/10.1175/2011JTECHO830.1>, 2011.

516 Frenger, I., Bianchi, D., Stührenberg, C., Oschlies, A., Dunne, J., Deutsch, C., Galbraith, E., and Schütte, F.: Biogeochemical
517 role of subsurface coherent eddies in the ocean: Tracer cannonballs, hypoxic storms, and microbial stewpots?, *Global*
518 *Biogeochem. Cycles*, 32, 226–249, <https://doi.org/10.1002/2017GB005743>, 2018.

519 Graham, F. S. and McDougall, T. J.: Quantifying the nonconservative production of conservative temperature, potential
520 temperature, and entropy, *J. Phys. Oceanogr.*, 43, 838–862, <https://doi.org/10.1175/JPO-D-11-0188.1>, 2013.

521 Gaillard, F., Autret, E., Thierry, V., Galaup, P., Coatanoan, C., and Loubrieu, T.: Quality control of large Argo datasets, *J.*
522 *Atmos. Oceanic Technol.*, 26, 337–351, <https://doi.org/10.1175/2008JTECHO552.1>, 2009.

523 GEBCO Compilation Group: GEBCO 2023 Grid, NERC EDS British Oceanographic Data Centre NOC [data set],
524 <https://doi.org/10.5285/f98b053b-0cbc-6c23-e053-6c86abc0af7b>, 2023.

525 Groeskamp, S., Griffies, S. M., Iudicone, D., Marsh, R., Nurser, A. J., and Zika, J. D.: The water mass transformation
526 framework for ocean physics and biogeochemistry, *Annu. Rev. Mar. Sci.*, 11, 271–305, <https://doi.org/10.1146/annurev-marine-010318-095421>, 2019.

527 Hanawa, K. and Talley, L. D.: Mode waters, *Int. Geophys.*, 77, 373–386, [https://doi.org/10.1016/S0074-6142\(01\)80129-7](https://doi.org/10.1016/S0074-6142(01)80129-7),
528 2001.

530 Herraiz-Borreguero, L. and Rintoul, S. R.: Subantarctic Mode Water: Distribution and circulation, *Ocean Dynam.*, 61, 103–
531 126, <https://doi.org/10.1007/s10236-010-0352-9>, 2011.

532 Hersbach, H., Bell, B., Berrisford, P., Hirahara, S., Horányi, A., Muñoz-Sabater, J., Nicolas, J., Peubey, C., Radu, R., Schepers,
533 D., Simmons, A., Soci, C., Abdalla, S., Abellán, X., Balsamo, G., Bechtold, P., Biavati, G., Bidlot, J., Bonavita, M., De Chiara,
534 G., Dahlgren, P., Dee, D., Diamantakis, M., Dragani, R., Flemming, J., Forbes, R., Fuentes, M., Geer, A., Haimberger, L.,
535 Healy, S., Hogan, R. J., Hólm, E., Janisková, M., Keeley, S., Laloyaux, P., Lopez, P., Lupu, C., Radnoti, G., de Rosnay, P.,
536 Rozum, I., Vamborg, F., Villaume, S., and Thépaut, J. N.: The ERA5 global reanalysis, *Q. J. Roy. Meteor. Soc.*, 146, 1999–
537 2049, <https://doi.org/10.1002/qj.3803>, 2020.

538 Ioannou, A., Guez, L., Laxenaire, R., and Speich, S.: Global assessment of mesoscale eddies with TOEddies: Comparison
539 between multiple datasets and colocation with in situ measurements, *Remote Sens.*, 16, 4336,
540 <https://doi.org/10.3390/rs16224336>, 2024.

541 Jackett, D. R. and McDougall, T. J.: An oceanographic variable for the characterization of intrusions and water masses, Deep-
542 Sea Res., 32, 1195–1207, [https://doi.org/10.1016/0198-0149\(85\)90003-2](https://doi.org/10.1016/0198-0149(85)90003-2), 1985.

543 Jutras, M., Bushinsky, S. M., Cerovečki, I., and Briggs, N.: Mixing accounts for more than half of biogeochemical changes
544 along mode water ventilation pathways, Geophys. Res. Lett., 52, e2024GL113789, <https://doi.org/10.1029/2024GL113789>,
545 2025.

546 Kalvelage, T., Lavik, G., Jensen, M. M., Revsbech, N. P., Lüscher, C., Schunck, H., Desai, D. K., Hauss, H., Kiko, R.,
547 Holtappels, M., LaRoche, J., Schmitz, R. A., Graco, M. I., and Kuypers, M. M. M.: Aerobic microbial respiration in oceanic
548 oxygen minimum zones, PLoS ONE, 10, e0133526, <https://doi.org/10.1371/journal.pone.0133526>, 2015.

549 Karstensen, J., Schütte, F., Pietri, A., Krahmann, G., Fiedler, B., Grundle, D., Hauss, H., Körtzinger, A., Lüscher, C. R., Testor,
550 P., Vieira, N., and Visbeck, M.: Upwelling and isolation in oxygen-depleted anticyclonic mode water eddies and implications
551 for nitrate cycling, Biogeosciences, 14, 2167–2181, <https://doi.org/10.5194/bg-14-2167-2017>, 2017.

552 Lacour, L., Llort, J., Briggs, N., Strutton, P. G., and Boyd, P. W.: Seasonality of downward carbon export in the Pacific
553 Southern Ocean revealed by multi-year robotic observations, Nat. Commun., 14, 1278, [https://doi.org/10.1038/s41467-023-36954-7](https://doi.org/10.1038/s41467-023-
554 36954-7), 2023.

555 Laxenaire, R., Guez, L., Chaigneau, A., Isic, M., Ioannou, A., and Speich, S.: TOEddies global mesoscale eddy atlas colocated
556 with Argo float profiles, SEANOE [data set], <https://doi.org/10.17882/102877>, 2024.

557 Lévy, M., Resplandy, L., Palter, J. B., Couespel, D., and Lachkar, Z.: The crucial contribution of mixing to present and future
558 ocean oxygen distribution, in: Ocean mixing, edited by: Meredith, M. and Naviera Garabato, A., Elsevier, 329–344,
559 <https://doi.org/10.1016/B978-0-12-821512-8.00020-7>, 2022.

560 Li, Z., England, M. H., and Groeskamp, S.: Recent acceleration in global ocean heat accumulation by mode and intermediate
561 waters, Nat. Commun., 14, 1–14, <https://doi.org/10.1038/s41467-023-42468-z>, 2023.

562 Liu, C. and Li, P.: The impact of meso-scale eddies on the Subtropical Mode Water in the western North Pacific, J. Ocean
563 Univ. China, 12, 230–236, <https://doi.org/10.1007/s11802-013-2223-8>, 2013.

564 McCartney, M. S.: The subtropical recirculation of mode waters, J. Mar. Res., 40, 427–464, 1982.

565 McDougall, T. J.: Potential enthalpy: A conservative oceanic variable for evaluating heat content and heat fluxes, J. Phys.
566 Oceanogr., 33, 945–963, [https://doi.org/10.1175/1520-0485\(2003\)033<0945:PEACOV>2.0.CO;2](https://doi.org/10.1175/1520-0485(2003)033<0945:PEACOV>2.0.CO;2), 2003.

567 McDougall, T. J. and Barker, P. M.: Getting started with TEOS-10 and the Gibbs Seawater (GSW) Oceanographic Toolbox,
568 SCOR/IAPSO WG127, 28 pp., ISBN 978-0-646-55621-5, 2011.

569 McDougall, T. J., Jackett, D. R., Millero, F. J., Pawlowicz, R., and Barker, P. M.: A global algorithm for estimating Absolute
570 Salinity, Ocean Sci., 8, 1117–1128, <https://doi.org/10.5194/os-8-1117-2012>, 2012.

571 McDougall, T. J. and Krzysik, O. A.: Spiciness, J. Mar. Res., 73, 141–152, <https://doi.org/10.1357/002224015816665589>,
572 2015.

573 Nurser, A. J. G., Marsh, R., and Williams, R. G.: Diagnosing water mass formation from air–sea fluxes and surface mixing, J.
574 Phys. Oceanogr., 29, 1468–1487, [https://doi.org/10.1175/1520-0485\(1999\)029<1468:DWMFFA>2.0.CO;2](https://doi.org/10.1175/1520-0485(1999)029<1468:DWMFFA>2.0.CO;2), 1999.

575 Portela, E., Kolodziejczyk, N., Vic, C., and Thierry, V.: Physical mechanisms driving oxygen subduction in the global ocean,
576 *Geophys. Res. Lett.*, 47, e2020GL089040, <https://doi.org/10.1029/2020GL089040>, 2020a.

577 Portela, E., Kolodziejczyk, N., Maes, C., and Thierry, V.: Interior water-mass variability in the Southern Hemisphere oceans
578 during the last decade, *J. Phys. Oceanogr.*, 50, 361–381, <https://doi.org/10.1175/JPO-D-19-0128.1>, 2020b.

579 Queste, B. Y., Vic, C., Heywood, K. J., and Piontkovski, S. A.: Physical controls on oxygen distribution and denitrification
580 potential in the north west Arabian Sea, *Geophys. Res. Lett.*, 45, 4143–4152. <https://doi.org/10.1029/2017GL076666>, 2018a.

581 Queste, B. Y., Heywood, K. J., and Piontkovski, S. A.: Exploring the potential of ocean gliders: A pirate-proof technique to
582 illuminate mesoscale physical–biological interactions off the coast of Oman (2015–2016), British Oceanographic Data Centre
583 – Natural Environment Research Council, UK [data set], <https://doi.org/10.5285/697eb954-f60c-603b-e053-6c86abc00062>,
584 2018b.

585 Resplandy, L., Lévy, M., Bopp, L., Echevin, V., Pous, S., Sarma, V. V. S. S., and Kumar, D.: Controlling factors of the oxygen
586 balance in the Arabian Sea's OMZ, *Biogeosciences*, 9, 5095–5109, <https://doi.org/10.5194/bg-9-5095-2012>, 2012.

587 Sarma, V. V. S. S. and Udaya Bhaskar, T. V. S.: Ventilation of oxygen to oxygen minimum zone due to anticyclonic eddies
588 in the Bay of Bengal, *J. Geophys. Res.-Biogeosci.*, 123, 2145–2153, <https://doi.org/10.1029/2018JG004447>, 2018.

589 Senafí, F. A., Anis, A., and Menezes, V.: Surface heat fluxes over the northern Arabian Gulf and the northern Red Sea:
590 Evaluation of ECMWF-ERA5 and NASA-MERRA2 reanalyses, *Atmosphere*, 10, 504,
591 <https://doi.org/10.3390/atmos10090504>, 2019.

592 Shi, F., Luo, Y., and Xu, L.: Volume and transport of eddy-trapped mode water south of the Kuroshio Extension, *J. Geophys.*
593 *Res.-Oceans*, 123, 8749–8761, <https://doi.org/10.1029/2018JC014176>, 2018.

594 Schütte, F., Karstensen, J., Krahmann, G., Hauss, H., Fiedler, B., Brandt, P., Visbeck, M., and Körtzinger, A.: Characterization
595 of “dead-zone” eddies in the eastern tropical North Atlantic, *Biogeosciences*, 13, 5865–5881, <https://doi.org/10.5194/bg-13-5865-2016>, 2016.

596 Thoppil, P. G.: Mesoscale eddy modulation of winter convective mixing in the northern Arabian Sea, *Deep-Sea Res. Pt. II*,
597 216, 105397, <https://doi.org/10.1016/j.dsr2.2024.105397>, 2024.

598 Trott, C. B., Subrahmanyam, B., Chaigneau, A., and Roman-Stork, H. L.: Eddy-induced temperature and salinity variability
599 in the Arabian Sea, *Geophys. Res. Lett.*, 46, 2734–2742, <https://doi.org/10.1029/2018GL081605>, 2019.

600 Walin, G.: On the relation between sea-surface heat flow and thermal circulation in the ocean, *Tellus*, 34, 187–195,
601 <https://doi.org/10.3402/tellusa.v34i2.10801>, 1982.

602 Weber, T. and Bianchi, D.: Efficient particle transfer to depth in oxygen minimum zones of the Pacific and Indian Oceans,
603 *Front. Earth Sci.*, 8, 567903, <https://doi.org/10.3389/feart.2020.00376>, 2020.

604 Xu, L., Li, P., and Xie, S.-P.: Observing mesoscale eddy effects on mode-water subduction and transport in the North Pacific,
605 *Nat. Commun.*, 7, 10505, <https://doi.org/10.1038/ncomms10505>, 2016.